Materials & Design 227 (2023) 111710

Contents lists available at ScienceDirect

Materials & Design

journal homepage: www.elsevier.com/locate/matdes

An ultra-strong and ductile crystalline-amorphous nanostructured surface layer on $TiZrHfTaNb_{0.2}$ high-entropy alloy by laser surface processing

Jiasi Luo [a,b], Wanting Sun [a], Dingshan Liang [b], Wenqing Yang [a], K.C. Chan [a], Fuzeng Ren [b,*], Xu-Sheng Yang [a,c,*]

[a] Department of Industrial and Systems Engineering, Research Institute for Advanced Manufacturing, The Hong Kong Polytechnic University, Hung Hom, Kowloon, Hong Kong, China
[b] Department of Materials Science and Engineering, Southern University of Science and Technology, Shenzhen 518055, China
[c] The Hong Kong Polytechnic University Shenzhen Research Institute, Shenzhen 518060, China

HIGHLIGHTS

- A crystalline-amorphous nanostructured top surface layer is developed on a high-entropy alloy by laser surface processing.
- The phase decomposition-mediated mechanisms forming the crystalline-amorphous nanostructured surface layer are uncovered.
- Localized micro-pillar compression tests on surface layer shows an ultrahigh yield strength and a good compression strain .
- The co-deformation cooperative actions include dislocation activities in nanograins but crystallization in amorphous GBs.
- The co-deformation cooperative effects subsequently lead to the grain coarsening via GB-mediated plasticity.

GRAPHICAL ABSTRACT

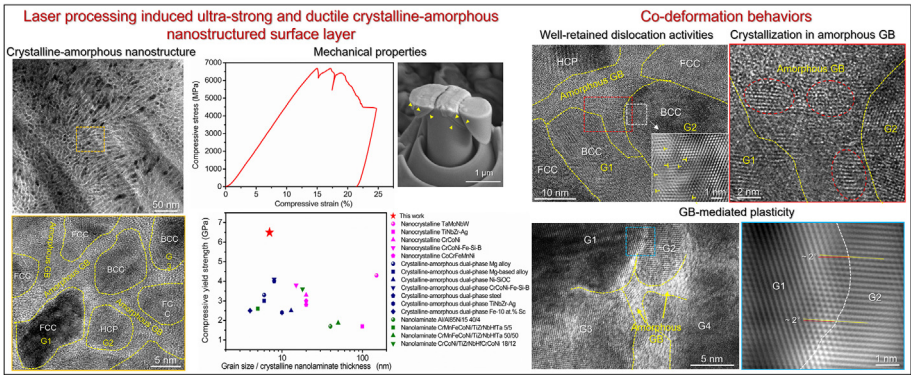

ARTICLE INFO

Article history:
Received 1 October 2022
Revised 21 December 2022
Accepted 6 February 2023
Available online 8 February 2023

Keywords:
Laser surface remelting
High-entropy alloy
Hetero-nanostructure
Crystalline-amorphous nanostructure
Micro-pillar compression tests

ABSTRACT

Heterogeneous crystalline-amorphous nanostructures have been documented to show superior strength-ductility synergy via the co-deformation cooperative effects of nanograins and amorphous grain boundaries. In this work, a facile laser surface remelting technique with rapid cooling rate was successfully developed to fabricate a ~ 100 μm-thick gradient nanostructured layer accompanied by phase decomposition on a $TiZrHfTaNb_{0.2}$ high-entropy alloy, where a ~ 5 μm-thick crystalline-amorphous nanostructured top surface layer with an average grain size of ~ 7 nm was obtained. Such crystalline-amorphous nanostructured layer shows an ultrahigh yield strength of ~ 6.0 GPa and a compression strain of ~ 25 % during the localized micro-pillar compression tests. The atomic observations reveal that co-deformation cooperative mechanisms include the well-retained dislocation activities in nanograins but crystallization in amorphous grain boundaries, which subsequently lead to the grain coarsening via grain boundary-mediated plasticity. This study sheds light on the development of high-performance

* Corresponding authors at: Department of Industrial and Systems Engineering, Research Institute for Advanced Manufacturing, The Hong Kong Polytechnic University, Hung Hom, Kowloon, Hong Kong, China (X.-S. Yang).
E-mail addresses: renfz@sustech.edu.cn (F. Ren), xsyang@polyu.edu.hk (X.-S. Yang).

https://doi.org/10.1016/j.matdes.2023.111710
0264-1275/© 2023 The Author(s). Published by Elsevier Ltd.
This is an open access article under the CC BY-NC-ND license (http://creativecommons.org/licenses/by-nc-nd/4.0/).

high-entropy alloys with novel crystalline-amorphous nanostructures and provides significant insight into their plastic deformation mechanisms.

© 2023 The Author(s). Published by Elsevier Ltd. This is an open access article under the CC BY-NC-ND license (http://creativecommons.org/licenses/by-nc-nd/4.0/).

1. Introduction

Strength and ductility are crucial properties of metals, but they are naturally exclusionary [1–4]. Metals could be either crystalline or amorphous (without long-range atomic order) structures. Generally, dislocation activities-dominated plasticity makes crystalline metals relatively soft but ductile, different from the ultrastrong but brittle amorphous counterparts without lattice dislocation slips [5,6]. Note that nanoscaling has diverse effects on the mechanical properties of crystalline and amorphous metals. Dislocation multiplication and motion are severely suppressed by the increased grain boundaries (GBs) in strengthened nanocrystalline (NC) metals (i.e. Hall-Petch relation [7,8]) would largely scarify their ductility [4,9–11]. A strengthening-softening transition (i.e. inverse Hall-Petch relation [12]) might be even triggered by fully GB-mediated plasticity in extremely-refined NC metals. In contrast, a brittle-to-ductile transition may happen in nanosized amorphous metals, owing to the inhomogeneous-to-homogeneous flow transition in shear bands against the localized failure [13]. Therefore, superior strength-ductility synergy has been recently obtained via the co-deformation cooperative effects in the constructed heterogeneous crystalline-amorphous nanostructures (e.g. NC "core" surrounded by nanosized amorphous "shell" GBs) [14–17].

Severe plastic deformation processes have been evidenced to cause the amorphization in NC metals for forming crystalline-amorphous nanostructures [16,18–21]. Besides, it could also be effectively generated through nanocrystallization in an amorphous matrix, such as sputtering [14,15,17] and laser processing techniques [22] with rapid cooling/solidification rates (10^5-10^8 K/s). In particular, the laser surface remelting (LSR) technique can offer the most rapid solidification/cooling rates at the outmost surface which are then gradually decayed to the inner region of the specimens. Therefore, the LSR technique could be developed to realize the crystalline-amorphous nanostructured surface layer on the generated gradient nanostructured (GNS) specimens [23–25].

High-entropy alloys (HEAs) composed of multi-principle elements (normally being single solid-solution or multi-phase crystalline structures) have drawn great attention due to their exceptional properties [26–29]. Noticeably, some crystalline HEAs could also form amorphous structures, especially for those with similar compositions (e.g. TiZrHfCuNi [30], CuNiPdPtP [31], and FeCrCoNi [22]). Therefore, a superior strength-ductility synergetic crystalline-amorphous nanostructured surface layer should also be expected to be constructed on HEA systems by the LSR technique. It was suggested that amorphous GBs can effectively impede and/or sink dislocation slips from nanograins; while dislocations accumulated in their interfaces can suppress the localized shear bands from amorphous GBs [15]. However, the formation process and so-called co-deformation cooperative actions (e.g. dislocations, possible further amorphization or crystallization [24,32,33], and heterogeneous characteristics) of the LSR-produced crystalline-amorphous nanostructured surface layer on HEA still need to be further verified and dissect at the atomic level.

Herein, a facile LSR technique was developed to fabricate a crystalline-amorphous nanostructured surface layer with an average grain size of $\sim$ 7 nm on a GNS TiZrHfTaNb$_{0.2}$ HEA by gradient phase decomposition. It shows an ultrahigh yield strength of $\sim$ 6.0 GPa and a compression strain of $\sim$ 25 % by the micro-pillar compression tests. High-resolution transmission electron microscope (HRTEM) observations reveal the co-deformation cooperative actions that include the well-retained dislocation activities in nanograins but crystallization in amorphous GBs, which subsequently lead to the grain coarsening via GB-mediated plasticity.

2. Experimental

2.1. Sample preparation

The TiZrHfTaNb$_{0.2}$ HEA was produced by vacuum arc melting using high-purity (>99.9 wt%) composing elements (i.e. Ti, Zr, Hf, Ta and Nb) with an atomic ratio of 1:1:1:1:0.2. A 2-kW fiber laser system (MSV-200 W, M−SOLV) was used to conduct the LSR process and thus generate a GNS surface layer on the as-cast plates under Ar shielding gas with a laser power of 90 W, a scanning speed of 30 mm/s, and beam spot size of 500 μm, as referred to our previous work [23].

2.2. Microstructure characterizations

The microstructure of the as-cast alloy was analyzed by electron backscatter diffraction (EBSD, Oxford, Nordlys Max2) equipped in a scanning electron microscope (SEM, TESCAN MIRA 3). The phase structures of the as-cast and laser-treated alloys at various depths were identified by X-ray diffraction (XRD) performed on a Rigaku Smartlab-9 kW diffractometer with Cu-Kα radiation (λ = 1.54 Å, 45 kV, 200 mA). The laser-treated specimen was first mechanically polished from the topmost surface to a certain target depth, then the grazing incident X-ray scattering (grazing angle ω = 1°) was adopted. Finally, a series of XRD measurements at different depth layers from the inner region to the topmost surface region was performed to measure the evolution of phase structures with decreasing depths in the laser-treated specimens. The cross-sectional microstructure of the laser-treated specimen was examined by a scanning electron microscope (SEM, TESCAN VEGA 3), and the microstructural evolution along the depth direction of the laser-treated specimen was systematically investigated by plane-view HRTEM (JEOL JEM-2100F), as well as high-angle annular dark-field scanning TEM (HAADF-STEM) equipped with energy-dispersive X-ray spectroscopy (EDS). Before the SEM cross-sectional examinations, the samples were first etched in the Kroll reagent (3 vol% HF and 6 vol% HNO_3) for 10–15 s. As for the sample preparation for the plane-view TEM observations at different depth layers, we first mechanically polished from the topmost surface side to a target depth layer and then polished from the opposite side, forming a TEM thin foil with a thickness of $\sim$ 25 μm. To ensure accuracy, a high-precision micrometer was used to measure the depth and thickness of samples. Finally, the prepared TEM thin foil at a target depth layer was further single-side ion thinned from the opposite side by using the precision ion polishing system (Gatan 691) before the TEM plane-view observations.

2.3. Hardness and Micro-pillar compression tests

The Vickers microhardness was measured along the depth direction of the laser-treated specimen under a load of 200 gf for 10 s on a microhardness tester (HXD-1000TMC/LCD). For the local-

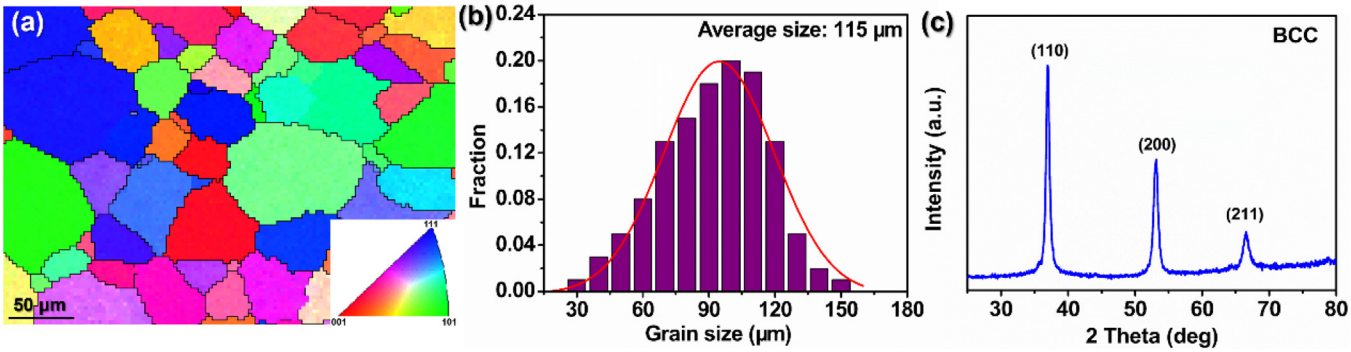

Fig. 1. Microstructure of the as-cast $TiZrHfTaNb_{0.2}$ HEA. (a) EBSD inverse pole figure. (b) Statistical grain size distribution, and (c) XRD pattern.

ized mechanical properties, we first prepared a series of micro-pillar samples with a diameter of Φ = 1 μm and a height of 2.5 μm (the aspect ratio was 2.5) at different depth layers along the depth direction in the laser-treated specimens by using the focused ion beam (FIB; Helios NanoLab™ 600i, FEI) milling system. Then, the micro-pillar compression tests were performed on a nanoindentation system (Hysitron TI950) at ambient temperature, which has a diamond flat-punch tip with Φ = 11 μm and is under the displacement control mode. For all compression tests, the total displacements of the nanoindentation tip were ~ 625 nm with a constant strain rate of 1×10^{-3} s^{-1}. Finally, the compressive engineering stress–strain curves along the depth direction could be obtained according to the measured force and displacement. Three independent micro-pillar compression tests were performed at each depth layer to maintain the experimental reliability. The TEM samples of compressed pillar were prepared by the FIB milling system.

3. Results

3.1. Microstructural evolution of the laser-treated $TiZrHfTaNb_{0.2}$ HEA

Fig. 1 displays the microstructure of the as-cast $TiZrHfTaNb_{0.2}$ HEA. It shows that the as-cast specimen has a body-centered-cubic (BCC) solid-solution phase (Fig. 1a) with an average grain size of ~ 115 μm (Fig. 1b), and the corresponding lattice constant is determined to be a = 3.345 Å. The cross-sectional microstructure of the laser-treated $TiZrHfTaNb_{0.2}$ HEA is shown by cross-sectional SEM image in Fig. 2a, which evidences a ~ 100 μm-thick GNS layer generated on the laser-treated specimen. This GNS layer is composed of submicron-sized dendrite grains with increasing domain size along the depth. The XRD patterns in Fig. 2b reveal that the original single BCC phase structure keeps at the depths of 55–65 μm. Face-centered-cubic (FCC, a_{fcc} = 4.910 Å) and minor hexagonal-close-packed (HCP, a_{hcp} = 3.180 Å, c = 5.030 Å) phases are gradually transformed when approaching the top surface, similar to our precious work [23]. Fig. 2c provide the refinement analysis of XRD patterns and variation of the full width at half maximum (FWHM) of BCC (1 1 0) with decreasing the depth, respectively. Accordingly, the calculated volume fraction of FCC phase gradually increases to as high as ~ 80 % at the topmost surface layer, where the large value of FWHM also implies the occurrence of amorphous phase.

Further plane-view TEM observations at different depths (Figs. 3-7) demonstrate the obvious grain refinement and phase transformation when approaching the topmost surface. To be specific, ultrafine equiaxed grains with an average grain size of ~ 270 nm are primarily formed at the depth of 40–60 μm (Fig. 3-a-b). It is found that the original single BCC phase is decomposed into another two BCC phases with compositional segregation (i.e. TiTaNb-rich and ZrHf-rich phases), as evidenced by the selected area electron diffraction (SAED) patterns and the corresponding STEM-HAADF image with EDS mapping in Fig. 3c-f. The SAED patterns in Fig. 3d-e show that two decomposed BCC phases have similar lattice constants of a = 3.35 Å, close to that of the original $TiZrHfTaNb_{0.2}$ BCC phase.

When the depth reduces to 20–40 μm, numerous FCC-structured lamellar precipitates with a lattice constant of a = 4.94 Å are found inside the ultrafine equiaxed matrix BCC

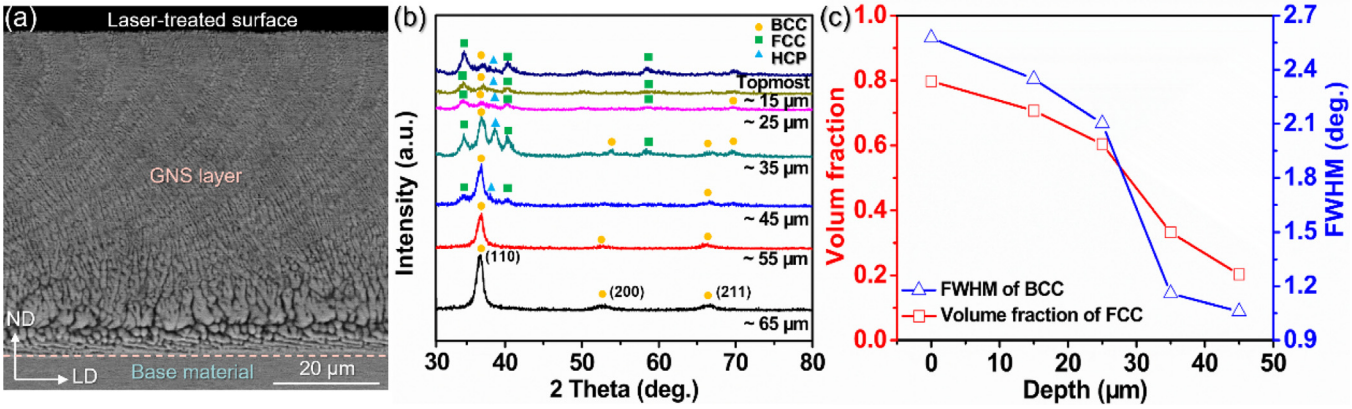

Fig. 2. (a) Cross-sectional SEM image showing the morphology along the depth direction of the laser-treated specimen. (b) XRD patterns of the laser-treated GNS layer at different depths. (c) Variations of the FWHM of BCC (1 1 0) and the volume fraction of FCC phase along the depth away from the topmost surface estimated via XRD refinement analysis.

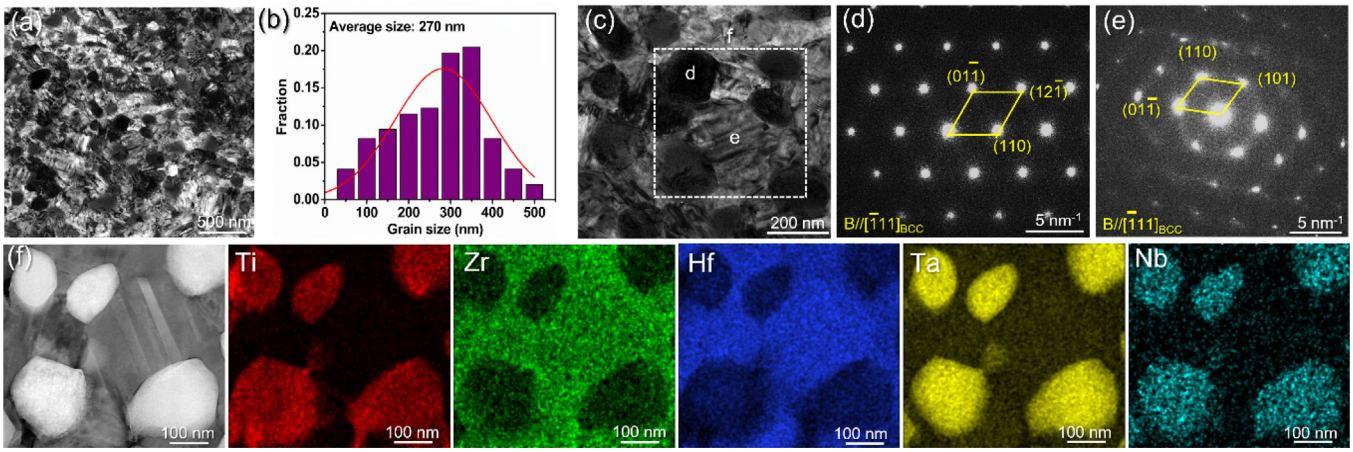

Fig. 3. Microstructure and composition of the GNS layer at the depth of 40–60 μm. (a) Bright-field TEM image. (b) Statistical grain size distribution. (c) High-magnification bright-field TEM image. (d-e) SAED patterns of grain d and e in (c), respectively. (f) STEM-HAADF image and EDS mapping of the selected region f in (c).

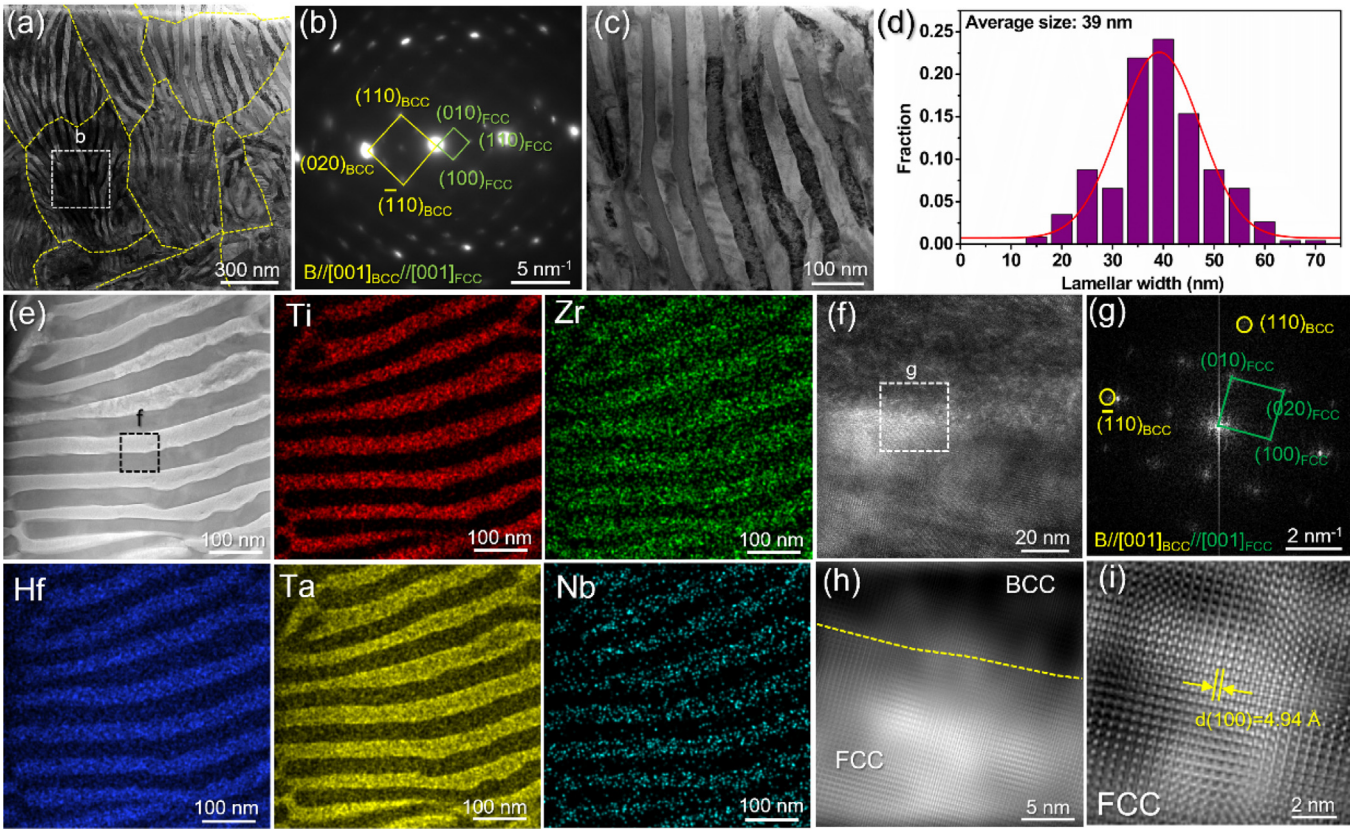

Fig. 4. Microstructure and composition of the GNS layer at the depth of 20–40 μm. (a) Bright-field TEM image. (b) SAED pattern of the selected area in (a). (c) High-magnification bright-field TEM image. (d) Statistical lamellar width distribution. (e) STEM-HAADF image and EDS mapping. (f) HRTEM image of adjacent BCC and FCC grains. (g) and (h) are corresponding FFT pattern and IFFT image of the selected area in (f). (i) IFFT image of FCC grain in (h).

grains, leading to a formation of specific alternating nano-lamellar microstructure with an average lamellar width of ~ 39 nm, as shown in Fig. 4a-d. The FCC lamellar precipitates are determined to be enriched by Zr and Hf elements, according to the STEM-HAADF mage with EDS mapping (Fig. 4e) and the HRTEM images associated with fast Fourier transform (FFT) patterns (Fig. 4f-i). The formation of the specific nano-lamellar structure should be related to the composition-segregation phase transformation during the LSR rapid cooling/solidification process [34]. In the rapid cooling/solidification process, the earlier formed composition-segregation phase and the later formed phase alternately facilitate the nucleation and growth of each phase at their interfaces, leading to the specific alternative layered eutectic structure at the nanoscale level [34,35].

At the depth layer of 10–20 μm, the above FCC nanolaminates are further refined to the finer nanostructure consisting of irregularly shaped aggregates or chains interconnected [36], as TEM images shown in Fig. 5a, forming the continuous network with an average size of ~ 35 nm (Fig. 5b). Apart from the pre-transformed ZrHf-rich FCC and matrix BCC phases (Fig. c-d), one

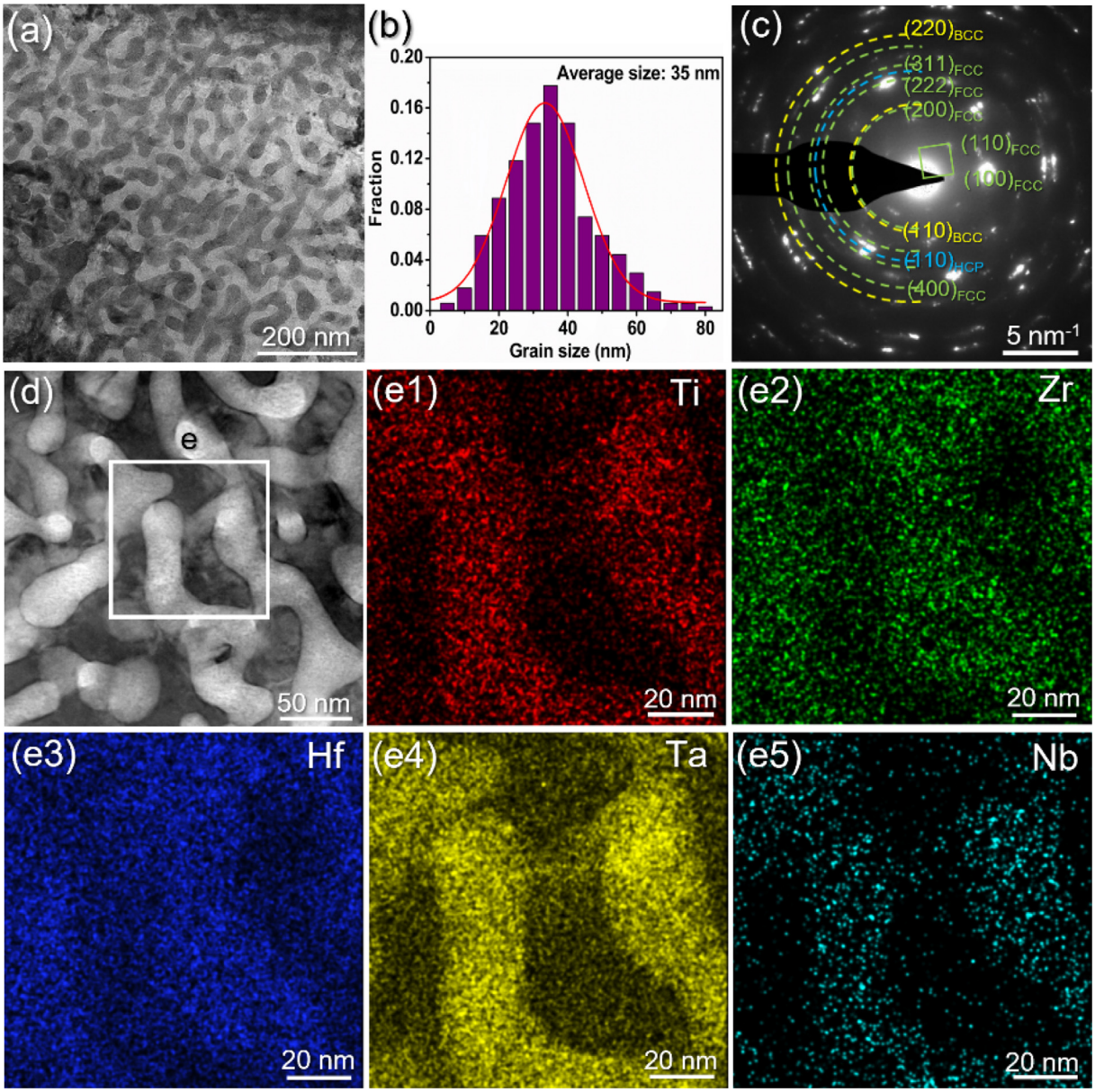

Fig. 5. Microstructure and composition of the GNS layer at the depth of 10–20 μm. (a) Bight-field TEM image. (b) Statistical grain size distribution. (c) Corresponding SAED pattern. (d) STEM-HAADF image. (e) EDS mapping of the selected area in (d).

diffraction ring for the HCP phase can also be indexed in the corresponding SAED pattern in Fig. 5c, indicating a low volume-fraction HCP phase formed in this depth.

It becomes a typical equiaxed nanograined structure with a continuously refined average grain size of ~ 14 nm at the depth of 5–10 μm (Fig. 6a-d). The atomic observations reveal the lattice constant of the HCP phase as a_{hcp} = 2.94 Å and c_{hcp} = 5.16 Å (Fig. 6e-f), in good agreement with the calculated results of XRD patterns.

More interestingly, at the top surface layer (depth of 0–5 μm), nanograins are found to be extremely refined to only ~ 7 nm, and embraced by thick amorphous GBs (Fig. 7a-c). It is confirmed by the SAED patterns composing of obvious amorphous diffraction ring in Fig. 7b and the typical HRTEM image (Fig. 7d), thereby verifying the heterogeneous crystalline-amorphous nanostructured surface layer on $TiZrHfTaNb_{0.2}$ HEA by the LSR technique. Consistent with the XRD results (Fig. 2b-c), nanograins (including dense decomposed FCC phase, few decomposed HCP phase, and BCC phase) and amorphous GBs can be well indexed by the atomic Fourier-filtered images and corresponding inverse FFT (IFFT) patterns in Fig. 7e-h. While the STEM-HAADF images with EDS mapping (Fig. 7i) and the captured linear elemental distribution (Fig. 7j) reveal that Ti, Zr, and Hf atoms tend to enrich in the amorphous GBs.

Accordingly, the variation of grain size along depth direction is summarized by Fig. 8, which indicates a gradual decrease from the ~ 115 μm of base material to only ~ 7 nm of the topmost surface layer. Meanwhile, the microhardness shows an inverse trend that the value increases from ~ 250 HV in the base material to ~ 660 HV (approximately 2.8 times) at the topmost surface, suggesting a significant surface strengthening effect after the LSR treatment. The results verified that the crystalline-amorphous nanostructure surface layer was formed on $TiZrHfTaNb_{0.2}$ HEA with GNS layer by LSR technique.

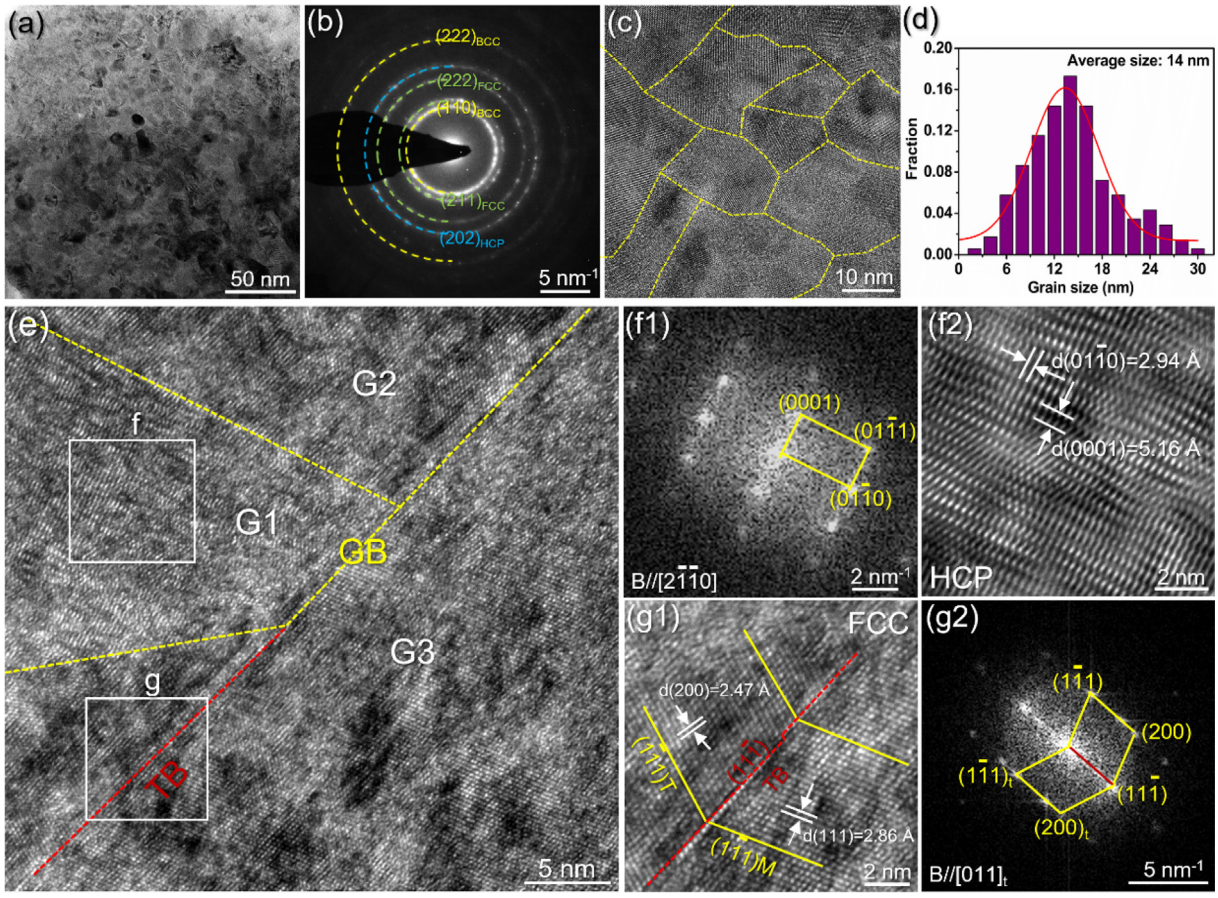

Fig. 6. Microstructure of the GNS layer at the depth of 5–10 μm. (a) Bight-field TEM image. (b) Corresponding SAED pattern. (c) HRTEM image showing the NGs. (c) Statistical grain size distribution. (e) HRTEM image of adjacent nanograins. (f) Corresponding FFT pattern and IFFT image of the selected area f in (e), showing the HCP phase at this depth. (g) The corresponding FFT pattern and IFFT image of the selected area g in (e), showing the FCC phase with twinning at this depth.

3.2. Localized mechanical properties

The specific mechanical properties at the different depth layer along the gradient direction of the laser-treated specimen were evaluated by localized micro-pillar compression tests, as shown in Fig. 9a. The yield strength of the base material is determined to be 1.1 ± 0.1 GPa. Attributed to the grain refinement and phase decomposition, the yield strength is obviously enhanced with the decrease of the depths. More specifically, the values of yield strength are examined to be 1.6 ± 0.2 GPa, 4.0 ± 0.6 GPa, 4.5 ± 0.5 GPa and 5.2 ± 0.7 GPa at the depth of 60 μm, 40 μm, 20 μm and 10 μm, respectively. Remarkably, the best strength-ductility combination is achieved in the crystalline-amorphous nanostructured surface layer with an ultrahigh strength up to 6.0 ± 0.5 GPa and a uniform compressive strain of ~ 25 %. To the best of our knowledge, it is stronger than the reported NC HEAs and crystalline-amorphous dual-phase nanostructured/nanolaminated alloys [14,15,17,25,37–44], as summarized in Fig. 9b, eliminating the inverse Hall-Petch effect. Fig. 9c gives the SEM morphologies of micro-pillars after compression tests. Particularly, a flat-barrel shape with slipping bands (signature of homogeneous plastic flow) can be obviously observed in the compressed crystalline-amorphous nanostructured micro-pillar, as the yellow arrows indicated in Fig. 9c1. Note that an obvious decrease in flow stress (i.e. softening behavior) occurs in the stress–strain curve of crystalline-amorphous surface specimen once its plastic strain is over ~ 17 %, implying a transition in the underlying micro-plastic mechanisms in the micro-pillar compressive tests.

4. Discussion

4.1. Phase decomposition-mediated formation of crystalline-amorphous nanostructure and GNS surface layer

As reported in our previous work [23], phase decomposition-mediated gradient refinement mechanisms were believed to facilitate forming the GNS layer on the TiZrHfTaNb-based HEA, owing to the selected LSR technique that could induce gradient distribution of solidification/cooling rates along the depth direction. More specifically, the high-energy LSR process could most effectively melt the outmost surface region (i.e. amorphous status), which will also receive the highest cooling rate (e.g. only tens of milliseconds for the whole cooling duration). Therefore, the crystallization in the following solidification process might only be partially completed, so as to form the crystalline-amorphous nanostructure. Especially, on the topmost surface having the highest cooling rate, crystallization is greatly suppressed [45]. In addition to the cooling rate, chemical compositions could also influence the Gibbs free energy and kinetics status during the crystallization process [45]. In contrast to the laser-treated TiZrHfTaNb HEA with no amorphous phase in our previous work [23], the laser-treated $TiZrHfTaNb_{0.2}$ HEA in the present work under the LSR parameters forms a crystalline-amorphous nanostructured topmost surface layer. It is therefore believed that the reduction of Nb element could enhance the glass-forming ability [45]. More specifically, in the surface layer with the highest cooling rate, the area rich in Ti, Zr, and Hf is prone to have high the glass-forming ability and thus

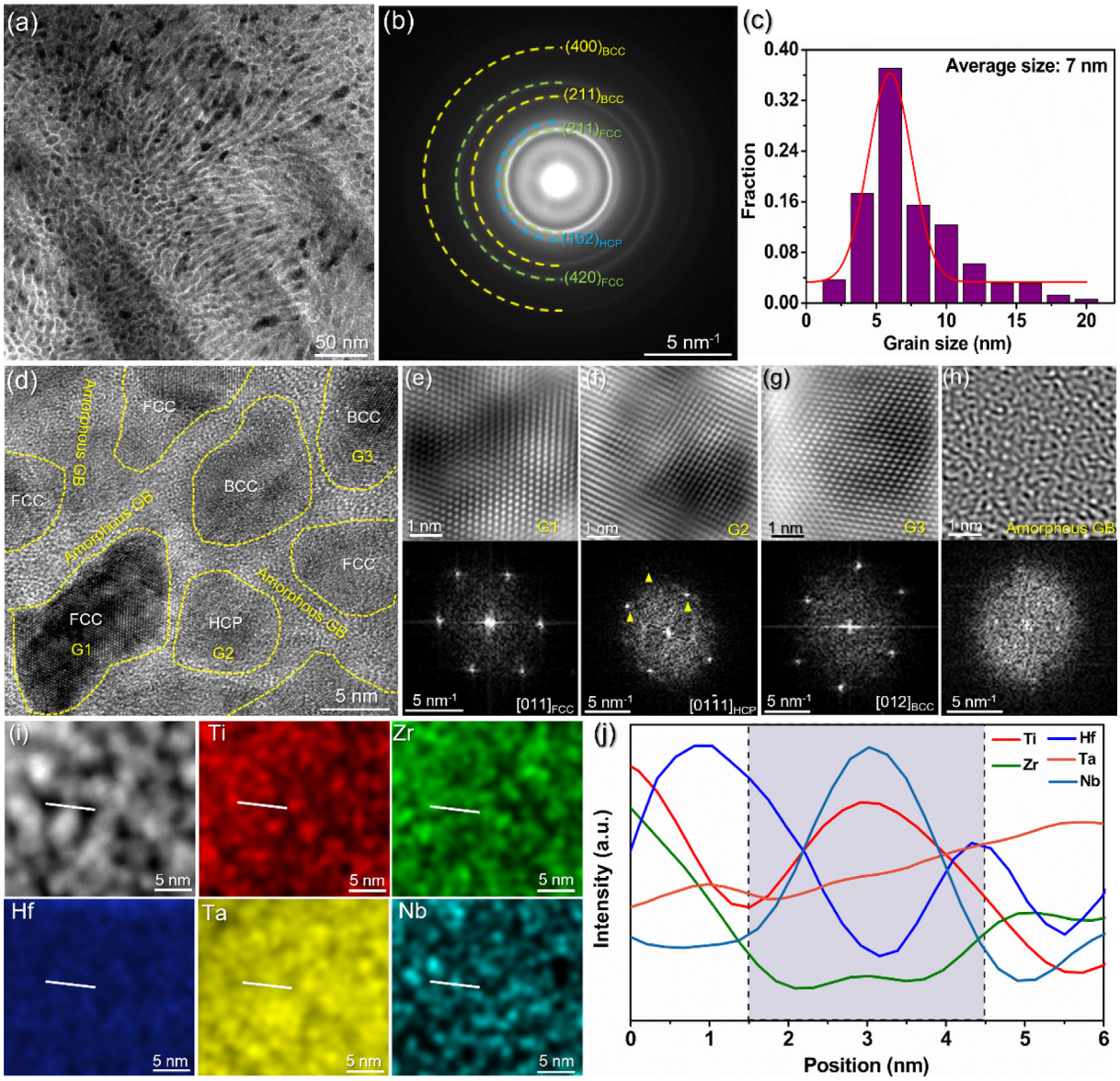

Fig. 7. Microstructure and composition of crystalline-amorphous nanostructured surface layer. (a) Bight-field TEM image. (b) Corresponding SAED pattern. (c) Statistical grain size distribution. (d) A representative HRTEM image showing that nanograins are embraced by amorphous GBs and (e-h) the corresponding FFT patterns and IFFT images of FCC, HCP, BCC nanograins, and amorphous GB in (d). (i) STEM-HAADF image and EDS mapping. (j) Line profiles of the elemental distribution along the white line marked in (i).

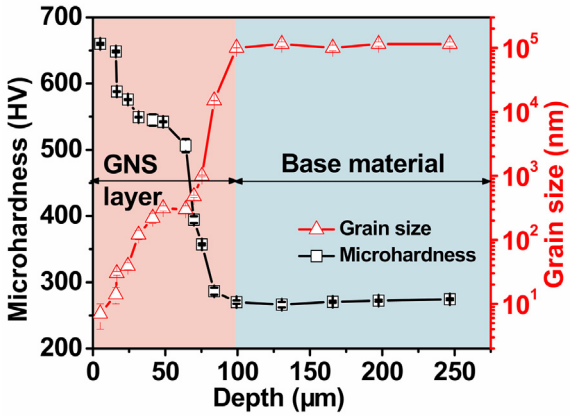

Fig. 8. Variations of grain size and microhardness along the depth away from the topmost surface.

solidify to a metastable amorphous phase [45]. On the other hand, the area rich in Ta and Nb tends to nucleate and crystallize to nanograins in the subsequently limited grain growth duration. Therefore, it is rational that the heterogeneous nanostructure of TaNb-rich nanograins embraced by TiZrHf-rich amorphous GBs was developed by the LSR technique, as evidenced in Fig. 7.

In addition, the composition-segregation phase decompositions play important role in the formation of the LSR-induced GNS layer, in which the phase decomposition sequence of "$TiZrHfTaNb_{0.2}$ BCC → TiTaNb-rich BCC 1 + ZrHf-rich BCC 2 → TiTaNb-rich BCC 1 + ZrHf-rich FCC → TiTaNb-rich BCC 1 + ZrHf-rich FCC + minor HCP" occurs along the depth direction from the matrix inner region to the topmost surface region. Such phase transformation should be related to the evolution of phase stability to accommodate the gradient LSR-induced thermal distributions (i.e. temperature and cooling rate) along the depth direction. The matrix TiZrHfTaNb HEA with the original BCC structure has been demonstrated to be

metastable, especially when changing temperatures [46–49]. The compositional segregation is likely to occur during the thermal process of LSR. Note that atomic sizes between the Zr and Hf atoms, as well as among another three atoms (Ti, Ta, and Nb) are almost equivalent in the $TiZrHfTaNb_{0.2}$ HEA system [50]. Besides, Ta and Nb with the highest melting points and sluggish diffusion would stabilize the BCC structure [47,49,51,52], while Zr and Hf are the least BCC-stabilizing elements [51]. Thus, the composition-segregation status in TiTaNb-rich BCC and ZrHf-rich metastable phases could be respectively favored and maintained during the phase transformation process at the different depth layers having different thermal statuses [46]. To be specific, the initial ZrHf-rich BCC phase could be transformed into two FCC phases with the same composition-segregation status of ZrHf-rich [51], when approaching the topmost surface with higher temperatures during LSR. And the fine HCP precipitates can also be generated at the top surface areas with the highest temperature [48]. Meanwhile, the rapid and gradient cooling rates during the LSR process lead to the gradient grain growth of newly formed phases, finally resulting in the formation of the GNS layer.

4.2. Deformation mechanism of crystalline-amorphous nanostructured surface layer

Microstructure characteristics of the compressed crystalline-amorphous nanostructured surface micro-pillars were studied by TEM observations (Fig. 10), to clarify the deformation mechanism of the specific LSR-produced crystalline-amorphous nanostructured surface layer. In the TEM image (Fig. 10a) taken in the topmost surface region of the compressed micro-pillar, severe plastic deformation behaviors (dislocation activities) are frequently observed in the deformed nanograins as indicated by the yellow arrows. It is also noted that the amorphous diffraction ring in SAED pattern (Fig. 10b) is much weaker than that before deformation (Fig. 7b). The average grain size of nanograins is increased to ~ 25 nm (Fig. 10c-d), relative to the original LSR-produced crystalline-amorphous nanostructured surface with a grain size of ~ 7 nm (Fig. 7c). It suggests a grain coarsening behavior accompanied by amorphous phase reduction in the crystalline-amorphous nanostructures after large plasticity.

To be more specific, atomic-scale images were further captured and presented in Fig. 10e-k to depict the underlying micro-plastic co-deformation cooperative mechanisms. On the one hand, Fig. 10e provides the HRTEM images of the compressed specimen including several adjacent nanograins and amorphous GBs. Dense full dislocations can be indexed in the atomic Fourier-filtered image inserted in Fig. 10e to nucleate and/or pin at the BCC nanograin-amorphous GB interfaces. While different dislocation activities (stacking faults (SFs) and deformation twinning) mainly via partial dislocations are found to emit from the FCC nanograin-amorphous GB interfaces and across the interior of nanograin, as shown in Fig. 10g-h. The above-characterized dislocation activities are well consistent with the observed features in Fig. 10a. In contrast to the softening behavior in extremely-refined nanograins (inverse Hall-Petch effect [12]), amorphous GBs have been suggested to act as strong barriers to effectively impede and/or sink dislocation slips from nanograins, thereby contributing to a significant strengthening effect (Fig. 9a) with dislocations accumulated at the nanograin-amorphous interfaces [41,53]. The crystallization is reported to contribute to certain plasticity during the deformation of crystalline-amorphous structure [21,54]. On the other hand, both Fig. 10f and j show that clusters of lattice fringes with short-range order are formed inside amorphous GBs. It was suggested that dislocations accumulated at the nanograin-amorphous interfaces can suppress the localized shear bands from amorphous GBs [15]. Noteworthy, it might decrease the activation energy for crystallization [33,55] and facilitate the creation of free volume and stimulate localized atomic dilatation [56]. Consequently, it likely induces the crystallization in amorphous structures, especially triggering at the nanograin-amorphous interfaces under

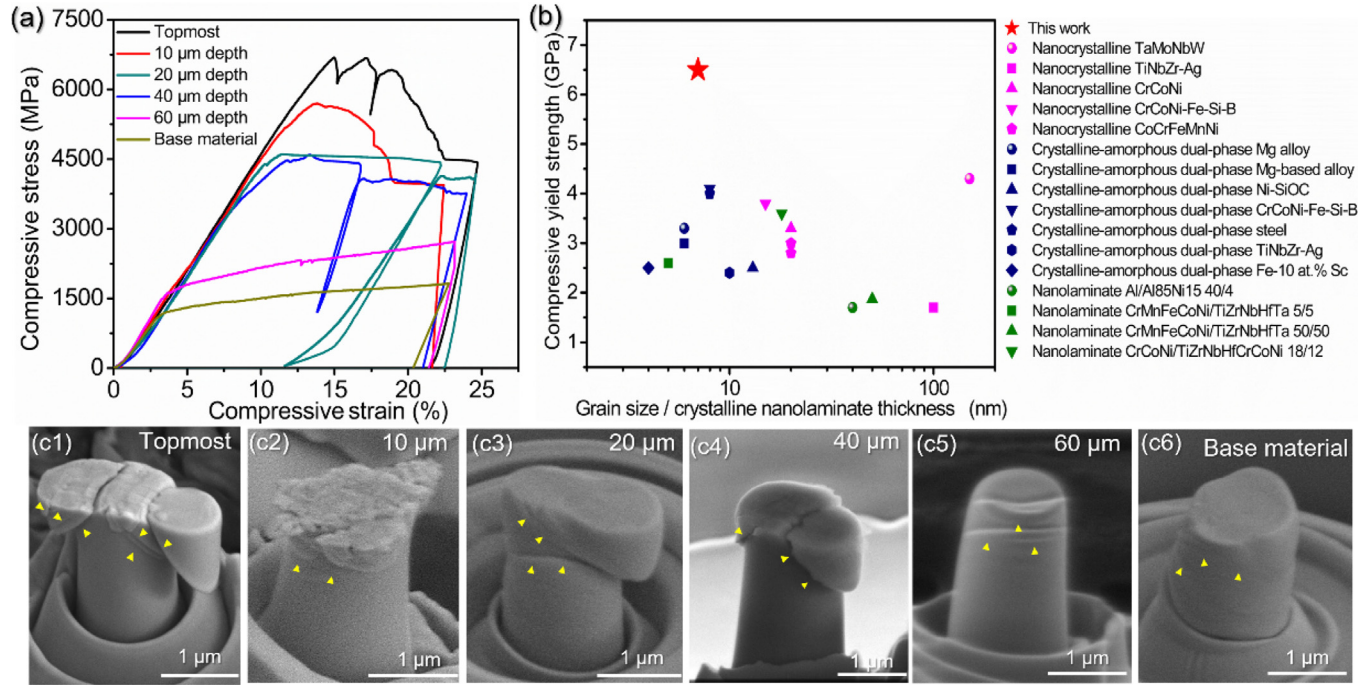

Fig. 9. Localized mechanical properties of the laser-treated specimen by micro-pillar compressive tests. (a) Typical engineering stress–strain curves of micro-pillars with 1 μm-diameter at different depths. (b) A comparison of the compressive yield strength between the present crystalline-amorphous nanostructured HEA and some reported nanocrystalline M/HEAs, crystalline-amorphous dual-phase alloys, and nanolaminate alloys. (c) Typical SEM images showing the compressed micro-pillars at different depths.

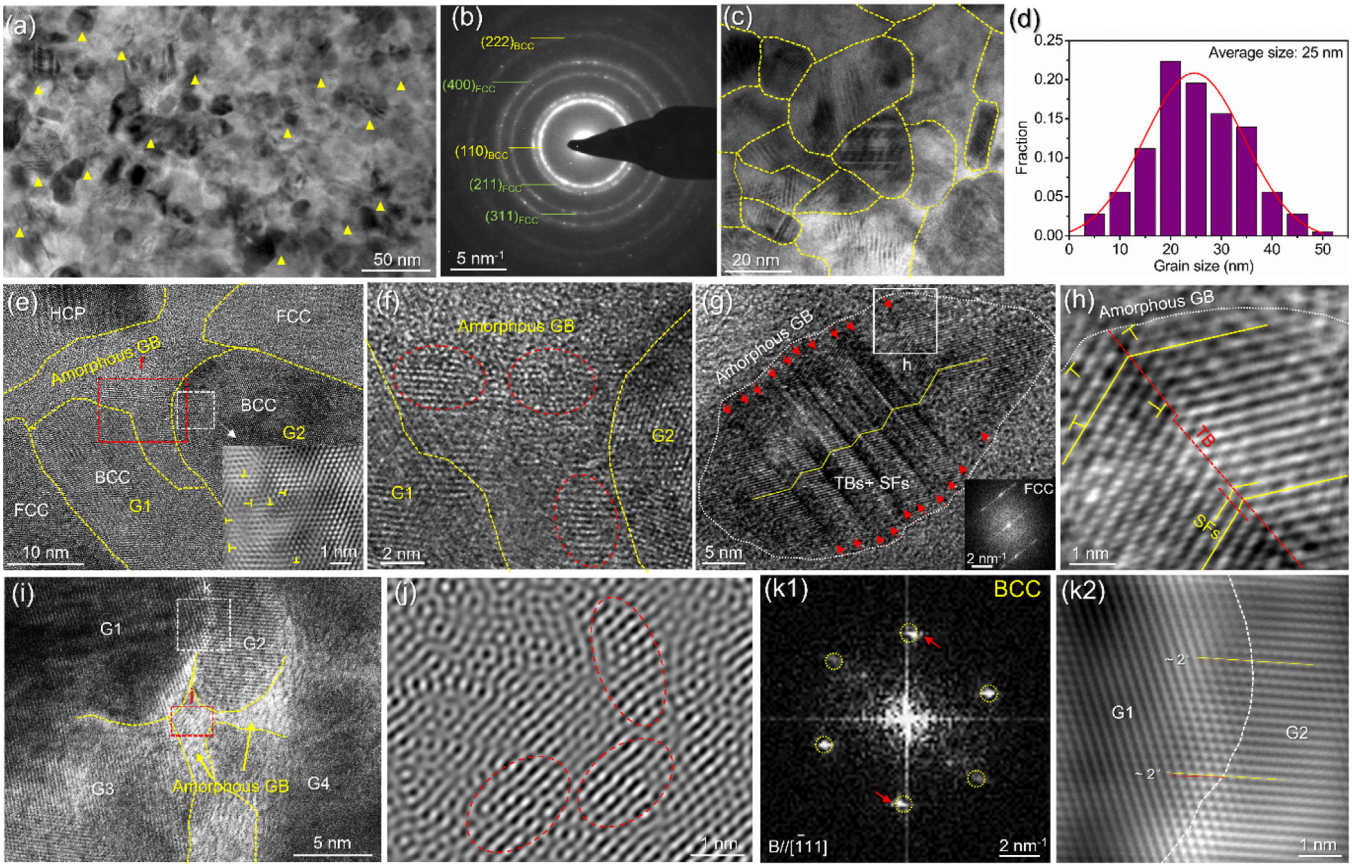

Fig. 10. Microstructure of the compressed micro-pillar at the topmost surface of the laser-treated specimen. (a-b) Bright-field TEM image and corresponding SAED pattern, where yellow arrows indicate the plastic deformation of the nanograins. (c) Enlarged bright-field TEM image. (d) Statistical grain size distribution. (e) An HRTEM image of several adjacent deformed nanograins and amorphous GB, with inset showing the IFFT image of the selected region near GB of BCC nanograin containing numbers of dislocations. (f) Enlarged HRTEM image of the rectangle region f in (e), showing the lattice with short-range order in deformed amorphous GB. (g) A typical HRTEM image of FCC nanograin containing high-density deformation twinning and SFs, with inset showing the corresponding FFT pattern. (h) IFFT image of the selected area in (g), showing the interface between the FCC nanograin and its surrounding amorphous GB. (i) An HRTEM image of several adjacent deformed nanograins and amorphous GB. (f) IFFT image of the selected region j in (i), showing the lattice with short-range order in deformed amorphous GB. (k) FFT pattern and corresponding IFFT image of the selected region k in (i), showing two adjacent nanograins with a small misorientation of ~ 2° and implying the grain rotation induced-grain coarsening process through GB-mediated plasticity. (For interpretation of the references to colour in this figure legend, the reader is referred to the web version of this article.)

high-stress concentration [32,56,57], as evidenced in Fig. 10f and j. Accordingly, the co-deformation cooperative actions including the retained dislocation activities in nanograins but crystallization in amorphous GBs could contribute to an ultrahigh yield strength with strength-ductility synergy (e.g. an initial homogenous plastic strain of ~ 17 % in Fig. 9a). At last, the crystallization process would decrease the volume fraction of amorphous GBs and thus transit more crystalline-crystalline interfaces. It should be noted that the typical GB-mediated mechanisms (e.g. GB sliding, GB migration, and grain rotation) [58–61] in extreme-refined nanograins (i.e. softening effect) would dominate the further compressive plastic deformation. Accordingly, the upper region in Fig. 10i presents two adjacent nanograins (G1 and G2), showing a crystalline-crystalline interface with a small misorientation of ~ 2° (Fig. 10*k*). It could be related to the GB-mediated plasticity through grain rotation and subsequently be responsible for the grain coarsening, as observed in Fig. 10a-d. In this connection, the softening behavior is also observed from the stress–strain curve of crystalline-amorphous surface specimen once its plastic strain exceeds ~ 17 % (Fig. 9a). As concluded, the well-retained dislocation activities in nanograins but crystallization in amorphous grain boundaries contribute the large plasticity in the crystalline-amorphous nanostructure, but it ultimately leads to the softening effect caused by the grain coarsening via grain boundary-mediated plasticity.

5. Conclusions

In summary, a facile LSR technique is developed to fabricate a crystalline-amorphous nanostructured surface layer on a GNS $TiZrHfTaNb_{0.2}$ HEA by gradient phase decomposition. The mechanical property is evaluated by localized micro-pillar compression tests, which show the good strength-ductility combination in the crystalline-amorphous nanostructured surface layer with an ultrahigh strength up to ~ 6.0 GPa and a compression strain of ~ 25 %. Atomic observations reveal that the co-deformation cooperative mechanisms include the well-retained dislocation activities in nanograins but crystallization in amorphous grain boundaries, which subsequently lead to the grain coarsening via grain boundary-mediated plasticity. The large plasticity achieved in the localized micro-pillar compressive tests on the LSR-produced crystalline-amorphous nanostructured surface layer on $TiZrHfTaNb_{0.2}$ HEA with an unprecedented yield strength allows us to uncover a novel underlying micro-plastic co-deformation cooperative mechanism.

Data availability

The raw/processed data required to reproduce these findings are available from the corresponding author upon reasonable request.

CRediT authorship contribution statement

Jiasi Luo: Validation, Investigation, Visualization, Writing – original draft. **Wanting Sun:** Investigation, Writing – original draft. **Dingshan Liang:** Investigation, Writing – original draft. **Wenqing Yang:** Investigation, Writing – original draft. **K.C. Chan:** Resources, Supervision. **Fuzeng Ren:** Methodology, Resources, Writing – review & editing, Supervision, Project administration, Funding acquisition. **Xu-Sheng Yang:** Conceptualization, Methodology, Resources, Writing – review & editing, Supervision, Project administration, Funding acquisition.

Data availability

The authors do not have permission to share data.

Declaration of Competing Interest

The authors declare that they have no known competing financial interests or personal relationships that could have appeared to influence the work reported in this paper.

Acknowledgements

This work was supported by the National Natural Science Foundation of China Projects (No. 51971187 and No. 52122102), Guangdong Basic and Applied Basic Research Foundation (No. 2022A1515011322). JL was supported by the joint PhD program of The Hong Kong Polytechnic University and Southern University of Science and Technology. JL and WY were supported by the grants from the Research Committee of PolyU under student account codes RK2N and RK3J, respectively.

References

[1] R. Valiev, Y. Estrin, Z. Horita, T.G. Langdon, M.J. Zehetbauer, Y. Zhu, Fundamentals of Superior Properties in Bulk NanoSPD Materials, Mater. Res. Lett. 4 (2015) 1–21.
[2] Q. Lu, Y. Shen, X. Chen, L. Qian, K. Lu, Ultrahigh Strength and High Electrical Conductivity in Copper, Science 304 (2004) 422–426.
[3] X. Wu, M. Yang, F. Yuan, G. Wu, Y. Wei, X. Huang, Y. Zhu, Heterogeneous lamella structure unites ultrafine-grain strength with coarse-grain ductility, Proc. Natl. Acad. Sci. U. S. A. 112 (2015) 1517193112.
[4] Y. Wang, M. Chen, F. Zhou, E. Ma, High tensile ductility in a nanostructured metal, Nature 419 (2002) 912–915.
[5] C. Schuh, A. Lund, Atomistic basis for the plastic yield criterion of metallic glass, Nat. Mater. 2 (2003) 449–452.
[6] Y. Zhang, A. Greer, Thickness of shear bands in metallic glasses, Appl. Phys. Lett. 89 (2006) 071907-071907.
[7] E.O. Hall, The Deformation and Ageing of Mild Steel: III Discussion of Results, Proc. Phys. Soc. London, Sect. B 64 (9) (1951) 747–753.
[8] N. Petch, The Cleavage Strength Of Polycrystals, J. Iron Steel Inst. Lond. 173 (1953) 25–28.
[9] X. Huang, N. Hansen, N. Tsuji, Hardening by Annealing and Softening by Deformation in Nanostructured Metals, Science 312 (2006) 249–251.
[10] R. Valiev, Nanostructuring of metals by severe plastic deformation for advanced properties, Nat. Mater. 3 (2004) 511–516.
[11] M. Wang, C. Tasan, D. Ponge, A. Kostka, D. Raabe, Smaller is less stable: Size effects on twinning vs. transformation of reverted austenite in TRIP-maraging steels, Acta Mater. 79 (2014) 268–281.
[12] K.A. Padmanabhan, G. Dinda, H. Hahn, H. Gleiter, Inverse Hall-Petch Effect and Grain Boundary Sliding Controlled Flow in Nanocrystalline Materials, Mater. Sci. Eng. A 452 (2007) 462–468.
[13] D. Jang, J. Greer, Transition From a Strong-Yet-Brittle to a Stronger-and-Ductile State by Size Reduction of Metallic Glasses, Nat. Mater. 9 (2010) 215–219.
[14] G. Wu, K.-C. Chan, L. Zhu, L. Sun, J. Lu, Dual-phase nanostructuring as a route to high-strength magnesium alloys, Nature 546 (2017) 80–83.
[15] G. Wu, S. Balachandran, B. Gault, W. Xia, C. Liu, Z. Rao, Y. Wei, S. Liu, J. Lu, M. Herbig, W. Lu, G. Dehm, Z. Li, D. Raabe, Crystal-Glass High-Entropy Nanocomposites with Near Theoretical Compressive Strength and Large Deformability, Adv. Mater. 32 (2020) 2002619.
[16] C. Liu, Y. Liu, Q. Wang, X. Liu, Y. Bao, G. Wu, J. Lu, Nano-Dual-Phase Metallic Glass Film Enhances Strength and Ductility of a Gradient Nanograined Magnesium Alloy, Adv. Sci. 7 (2020) 2001480.
[17] G. Wu, C. Liu, L. Sun, Q. Wang, B. Sun, B. Han, J.-J. Kai, J. Luan, T. Chain, K. Liu, L. Cao, J.L. Cheng, Hierarchical nanostructured aluminum alloy with ultrahigh strength and large plasticity, Nat. Commun. 10 (2019) 5099.
[18] R. Hebert, J. Perepezko, H. Rösner, G. Wilde, Deformation-driven catalysis of nanocrystallization in amorphous Al alloys, Beilstein J. Nanotechnol. 7 (2016) 1428–1433.
[19] G.Z. Ma, K. Song, B. Sun, Z.J. Yan, U. Kühn, C. Ding, J. Eckert, Effect of cold-rolling on the crystallization behavior of a CuZr-based bulk metallic glass, J. Mater. Sci. 48 (2013) 6825–6832.
[20] A.R. Yavari, W. Botta, C. Rodrigues, C. Cardoso, R. Valiev, Nanostructured bulk Al90Fe5Nd5 prepared by cold consolidation of gas atomised powder using severe plastic deformation, Scripta Mater. 46 (2002) 711–716.
[21] Q. Fang, F. Liu, H. Feng, P. Liaw, L. Jia, Microstructure evolution and deformation mechanism of amorphous/crystalline high-entropy-alloy composites, J. Mater. Sci. Technol. 54 (2020) 14–19.
[22] H. Chen, H.-Z. Cui, D. Jiang, X. Song, L. Zhang, G. Ma, X. Gao, H. Niu, X. Zhao, J. Li, C. Zhang, R. Wang, X. Sun, Formation and Beneficial Effects of the Amorphous/Nanocrystalline Phase in Laser Remelted (FeCoCrNi)75Nb10B8Si7 High-Entropy Alloy Coatings Fabricated by Plasma Cladding, J. Alloys Compd. 899 (2021) 163277.
[23] J. Luo, W. Sun, R. Duan, W. Yang, K.C. Chan, F. Ren, X.-S. Yang, Laser surface treatment-introduced gradient nanostructured TiZrHfTaNb refractory high-entropy alloy with significantly enhanced wear resistance, J. Mater. Sci. Technol. 110 (2022) 43–56.
[24] S. Jiang, Z. Mao, Y. Zhang, H. Li, Mechanisms of nanocrystallization and amorphization of NiTiNb shape memory alloy subjected to severe plastic deformation, Procedia Eng. 207 (2017) 1493–1498.
[25] W. Sun, J. Luo, Y.Y. Chan, J.H. Luan, X.-S. Yang, An extraordinary-performance gradient nanostructured Hadfield manganese steel containing multi-phase nanocrystalline-amorphous core-shell surface layer by laser surface processing, J. Mater. Sci. Technol. 134 (2023) 209–222.
[26] J.W. Yeh, S.K. Chen, S.J. Lin, J.Y. Gan, T.S. Chin, T.T. Shun, C.H. Tsau, S.Y. Chang, Nanostructured High-Entropy Alloys with Multiple Principal Elements: Novel Alloy Design Concepts and Outcomes, Adv. Eng. Mater. 6 (5) (2004) 299–303.
[27] B. Cantor, I. Chang, P. Knight, A.J.B. Vincent, Microstructural development in equiatomic multicomponent alloys, Mater. Sci. Eng. A 375–377 (2004) 213–218.
[28] D. Miracle, O. Senkov, A critical review of high entropy alloys and related concepts, Acta Mater. 122 (2016) 448–511.
[29] E. Ma, X. Wu, Tailoring heterogeneities in high-entropy alloys to promote strength–ductility synergy, Nat. Commun. 10 (2019) 5623.
[30] L. Ma, L. Wang, T. Zhang, A. Inoue, Bulk Glass Formation of Ti–Zr–Hf–Cu–M (M=Fe Co, Ni) Alloys, Mater. Tran. 43 (2002) 277–280.
[31] A. Takeuchi, N. Chen, T. Wada, Y. Yokoyama, H. Kato, A. Inoue, J.W. Yeh, Pd20Pt20Cu20Ni20P20 high-entropy alloy as a bulk metallic glass in the centimeter, Intermetallics 19 (2011) 1546–1554.
[32] S.-W. Lee, M. Huh, S. Chae, J.-C. Lee, Mechanism of the deformation-induced nanocrystallization in a Cu-based bulk amorphous alloy under uniaxial compression, Scripta Mater. 54 (2006) 1439–1444.
[33] W. Jiang, M. Atzmon, The effect of compression and tension on shear-band structure and nanocrystallization in amorphous Al90Fe5Gd5: A high-resolution transmission electron microscopy study, Acta Mater. 51 (2003) 4095–4105.
[34] X. Wen, X. Cui, G. Jin, Y. Liu, Y. Zhang, Y. Fang, In-situ synthesis of nano-lamellar Ni1.5CrCoFe0.5Mo0.1Nbx eutectic high-entropy alloy coatings by laser cladding: Alloy design and microstructure evolution, Surf. Coat. Tech. 405 (2021) 126728.
[35] M.E. Glicksman, Principles of solidification : an introduction to modern casting and crystal growth concepts, Springer, New York, 2011.
[36] X. Li, Z. Jin, Z. Xin, K. Lu, Constrained minimal-interface structures in polycrystalline copper with extremely fine grains, Science 370 (2020) 831–836.
[37] Y. Zou, H. Ma, R. Spolenak, Ultrastrong ductile and stable high-entropy alloys at small scales, Nat. Commun. 6 (2015) 7748.
[38] C. Liu, Z. Li, W. Lu, Y. Bao, W. Xia, X. Wu, H. Zhao, B. Gault, C. Liu, M. Herbig, A. Fischer, G. Dehm, G. Wu, D. Raabe, Reactive wear protection through strong and deformable oxide nanocomposite surfaces, Nat. Commun. 12 (2021) 5518.
[39] Z. Wang, C. Wang, Y. Zhao, Y.-C. Hsu, C.-L. Li, J.-J. Kai, C.-T. Liu, C.-H. Hsueh, High hardness and fatigue resistance of CoCrFeMnNi high entropy alloy films with ultrahigh-density nanotwins, Int. J. Plast. 131 (2020) 102726.
[40] G. Wu, L. Sun, L. Zhu, C. Liu, Q. Wang, Y. Bao, J. Lu, Near-ideal strength and large compressive deformability of a nano-dual-phase glass-crystal alloy in sub-micron, Scripta Mater. 188 (2020) 290–295.
[41] B. Wei, W. Wu, D. Xie, M. Nastasi, J. Wang, Strength, plasticity, thermal stability and strain rate sensitivity of nanograined nickel with amorphous ceramic grain boundaries, Acta Mater. 212 (2021) 116918.
[42] S. Katnagallu, G. Wu, S.P. Singh, S. Nandam, W. Xia, L. Stephenson, H. Gleiter, R. Schwaiger, H. Hahn, M. Herbig, D. Raabe, B. Gault, S. Balachandran, Nanoglass–nanocrystal composite – a novel material class for enhanced strength – plasticity synergy, Small 16 (2020) 2004400.
[43] G. Wu, C. Liu, A. Brognara, M. Ghidelli, Y. Bao, S. Liu, X. Wu, W. Xia, H. Zhao, J. Rao, D. Ponge, V. Devulapalli, W. Lu, G. Dehm, D. Raabe, Z. Li, Symbiotic crystal-glass alloys via dynamic chemical partitioning, Mater. Today 51 (2021) 6–14.
[44] L. Jiang, Z. Bai, M. Powers, Y. Fan, W. Zhang, E. George, A. Misra, Deformation mechanisms in crystalline-amorphous high-entropy composite multilayers, Mater. Sci. Eng. A 848 (2022) 143144.

[45] T. Wohlbier, Metallic Glasses and Their Composites, 2021.
[46] W. Wu, S. Ni, Y. Liu, M. Song, Effects of cold rolling and subsequent annealing on the microstructure of a HfNbTaTiZr high-entropy alloy, J. Mater. Res. 31 (2016) 3815–3823.
[47] O.N. Senkov, S.L. Semiatin, Microstructure and properties of a refractory high-entropy alloy after cold working, J. Alloys Compd. 649 (2015) 1110–1123.
[48] C. Yang, K. Aoyagi, H. Bian, A. Chiba, Microstructure evolution and mechanical property of a precipitation-strengthened refractory high-entropy alloy HfNbTaTiZr, Mater. Lett. 254 (2019) 46–49.
[49] B. Schuh, B. Völker, J. Todt, N. Schell, L. Perrière, J. Li, J.P. Couzinié, A. Hohenwarter, Thermodynamic instability of a nanocrystalline, single-phase TiZrNbHfTa alloy and its impact on the mechanical properties, Acta Mater. 142 (2018) 201–212.
[50] O.N. Senkov, J.M. Scott, S.V. Senkova, D.B. Miracle, C.F. Woodward, Microstructure and room temperature properties of a high-entropy TaNbHfZrTi alloy, J. Alloys Compd. 509 (2011) 6043–6048.
[51] M. Abdel-Hady, K. Hinoshita, M. Morinaga, General approach to phase stability and elastic properties of β-type Ti-alloys using electronic parameters, Scripta Mater. 55 (2006) 477–480.
[52] G.P. Tiwari, R.S. Mehrotra, Diffusion and melting, Defect and Diffusion, Forum 279 (2008) 23–37.
[53] Y. Wang, J. Li, A. Hamza, T. Barbee, Ductile crystalline-amorphous nanolaminates, Proc. Natl. Acad. Sci. U. S. A. 104 (2007) 11155–11160.
[54] J. Zhang, G. Liu, J. Sun, Crystallization-aided extraordinary plastic deformation in nanolayered crystalline Cu/amorphous Cu-Zr micropillars, Sci. Rep. 3 (2013) 2324.
[55] Z.X. Wang, F.Y. Li, M.X. Pan, D.Q. Zhao, Effects of high pressure on the nucleation of Cu60Zr20Hf10Ti10 bulk metallic glass, J. Alloys Compd. 388 (2005) 262–265.
[56] F. Spaepen, A Microscopic Mechanism for Steady State Inhomogeneous Flow in Metallic Glasses, Acta Metall. 25 (1977) 407–415.
[57] J. Kim, Y. Choi, S. Suresh, A. Argon, Nanocrystallization During Nanoindentation of a Bulk Amorphous Metal Alloy at Room Temperature, Science 295 (2002) 654–657.
[58] L. Wang, Y. Zhang, Z. Zeng, H. Zhou, J. He, P. Liu, M. Chen, J. Han, D.J. Srolovitz, J. Teng, Y. Guo, G. Yang, D. Kong, E. Ma, Y. Hu, B. Yin, X. Huang, Z. Zhang, T. Zhu, X. Han, Tracking the sliding of grain boundaries at the atomic scale, Science 375 (6586) (2022) 1261–1265.
[59] T. Rupert, D. Gianola, Y. Gan, K. Hemker, Experimental Observations of Stress-Driven Grain Boundary Migration, Science 326 (2009) 1686–1690.
[60] N. Okamoto, D. Kashioka, T. Hirato, H. Inui, Specimen- and Grain-Size Dependence of Compression Deformation Behavior in Nanocrystalline Copper, Int. J. Plast. 56 (2013) 171–183.
[61] T.H. Fang, N. Tao, K. Lu, Tension-induced softening and hardening in gradient nanograined surface layer in copper, Scripta Mater. 77 (2014) 17–20.